# $RE_2[B_2(SO_4)_6]$ (*RE* = Y, La–Nd, Sm, Eu, Tb–Lu): a silicate-analogous host structure with weak coordination behaviour†

Philip Netzsch,[a] Matthias Hämmer,[a] Peter Gross,[a] Harijs Bariss,[a] Theresa Block,[b] Lukas Heletta,[b] Rainer Pöttgen,[b] Jörn Bruns,‡[c] Hubert Huppertz[c] and Henning A. Höppe*[a]

The rare earth borosulfates $RE_2[B_2(SO_4)_6]$ with *RE* = Y, La–Nd, Sm, Eu and Tb–Lu were synthesised under solvothermal conditions starting from the metal chlorides (Pr, Nd, Eu), the metal oxides (Y, La, Ce, Sm, Tb, Dy, Er, Tm, Lu), or the metal powders (Ho, Yb). They crystallize isotypically with $Gd_2[B_2(SO_4)_6]$ in space group *C*2/*c* (*Z* = 4, *a* = 1346.9(3)–1379.24(17) pm, *b* = 1136.4(3)–1158.87(14) pm, *c* = 1079.9(3)–1139.54(14) pm, *β* = 93.369(8)–93.611(4)°). The anionic structure consists of an open-branched *vierer* single ring $\{oB, 1r\}[B_2S_2O_{12}(SO_3)_4]^{6-}$, similar to the mineral eakerite $(Ca_2Al_2Sn[Si_6O_{18}](OH)_2{\cdot}2H_2O)$ which contains $\{oB, 1r\}[Si_4O_{12}(SiO_3)_2]^{12-}$ moieties. The fluorescence spectroscopy of the samples with *RE* = Ce, Eu and Tb features emissions in the deep UV, the red, and the green part of the spectrum and furthermore revealed a weak coordination behaviour of the borosulfate anion. Thermal analysis of $Eu_2[B_2(SO_4)_6]$ showed the highest thermal stability observed for borosulfates so far; respective trends within the borosulfate family are discussed. Additionally, the compounds were characterised by magnetic measurements, vibrational and $^{151}$Eu Mößbauer spectroscopy.

## Introduction

Compounds consisting of a condensed network of tetrahedra $TX_4$ ($T$ = central atom, $X$ = terminal or bridging atom) are classified as silicate-analogous materials. By a partial or full formal substitution of the central silicon atom by aluminium, boron, or phosphorus alumosilicates or borophosphates can be obtained. Furthermore, the terminal or bridging oxygen atom can be substituted by nitrogen or sulfur leading to nitridosilicates and thiosilicates, respectively.

Within the search of new phosphor materials, silicate-analogous compounds are well suited host structures,[1,2] as high condensed structures often show low thermal quenching[2] and low Stokes shifts.[3] Prominent examples are materials doped with rare-earth ions like the nitridosilicate $Sr_2Si_5N_8:Eu^{2+}$,[4] the sialon $Ca_{0.625}Eu_x[Si_{0.75-3x}Al_{1.25+3x}O_xN_{16-x}]$,[5] or the borophosphate $Sr_6[B(PO_4)_4][PO_4]:Eu^{2+}$.[6]

A rather new class of silicate-analogous materials are borosulfates.[7] Such compounds can be considered as silicate-analogous in two ways: firstly, they comprise a network of corner-sharing borate and sulfate tetrahedra and secondly, the most common fundamental building unit $[B(SO_4)_4]^{5-}$ itself can be considered as a supertetrahedron with the borate unit as tetrahedral centre $T$ and the sulfate units as terminal or bridging moiety $X$. Indeed, striking similarities between the crystal structures of borosulfates and silicates have been observed; *e.g.* in $K_5[B(SO_4)_4]$[7] and the $[Si(SiO_4)_4]^{12-}$ supertetrahedra in *zunyite*, *viz.* $(Al_{13}Si_5O_{20}(OH, F)_{18}Cl)$,[8] are found or between *β-tridymite* and $Li[B(SO_4)_2]$,[9] in which lithium, boron and sulfur centred tetrahedra replace the $SiO_4$ tetrahedra, where a homeotypic relationship becomes obvious. With regard to borophosphates, some crystal structures are even isotypic like those of $K_3[B(SO_4)_3]$[9] and $Ba_3[B(PO_4)_3]$.[10] However, to the best of our knowledge, there are no rare earth borophosphates so far, except for doped compounds like $Sr_6[B(PO_4)_4][PO_4]:Eu^{2+}$.[6]

In contrast, further investigations on borosulfates led to the first rare earth borosulfate $Gd_2[B_2(SO_4)_6]$,[11] additionally also the non-condensed rare earth borate sulfate hydrates $RE(SO_4)[B(OH)_4](H_2O)_x$ (*RE* = Y, La, Pr, Nd, Sm–Lu) were published.[12] Recently, we studied the optical absorption properties of tran-

[a]*Lehrstuhl für Festkörperchemie, Universität Augsburg, Universitätsstraße 1, 86159 Augsburg, Germany. E-mail: henning.hoeppe@physik.uni-augsburg.de*
[b]*Institut für Anorganische und Analytische Chemie, Universität Münster, Corrensstrasse 30, 48149 Münster, Germany*
[c]*Institut für Allgemeine, Anorganische und Theoretische Chemie, Leopold-Franzens-Universität Innsbruck, Innrain 80–82, 6020 Innsbruck, Austria*
†Electronic supplementary information (ESI) available. See DOI: 10.1039/c9dt00445a
‡New adress: Institut für Anorganische Chemie, Universität zu Köln, Greinstraße 6, 50939 Köln, Germany

sition metal borosulfates and revealed a weak coordination behaviour as well as a weak nephelauxetic effect of borosulfate anions.[13] Since rare-earth ions normally are subject to very weak ligand-field effects, such compounds are good candidates of almost any compound class for an initial assessment of luminescent properties. Hence, we fully characterised the crystal structures of the rare earth borosulfates $RE_2[B_2(SO_4)_6]$ (*RE* = Y, La–Nd, Sm, Eu, Tb–Lu) with a focus on their luminescent properties, assisted by magnetic measurements and Mößbauer spectroscopy. We also elucidated their thermal stabilities.

## Results and discussion

### Synthetic approach

The synthesis of $Gd_2[B_2(SO_4)_6]$ was described as an acid base reaction starting from the superacid $H[B(HSO_4)_4]$ and anhydrous $GdCl_3$.[11] As the chlorides of the less basic rare earth metals are difficult to dehydrate, also other starting materials like rare earth oxides and rare earth metals are used as starting materials.[13] Therefore, chlorides ($PrCl_3$, $NdCl_3$, $EuCl_3$), oxides ($La_2O_3$, $CeO_2$, $Sm_2O_3$, $Tb_4O_7$, $Dy_2O_3$, $Er_2O_3$, $Tm_2O_3$, $Lu_2O_3$), and even metal powders (Ho, Yb) were used and yielded phase pure compounds (see Fig. S1 in the ESI†). Interestingly, the rare earth source influences the crystal size. By the use of rare earth chlorides, large single crystals with an edge length of several mm (Fig. 1) were obtained, whereas the use of oxides only yielded crystals with typical lengths of several hundred μm (Fig. S3 in the ESI†). This might be explained by the initial formation of rather stable chlorido-complexes controlling the concentration of available cations during crystallisation. Subsequently the crystallisation is enforced upon release of gaseous hydrogen chloride which has been proven to be an excellent "leaving group".[11]

### Crystal structure

The borosulfates $RE_2[B_2(SO_4)_6]$ (*RE* = Y, La–Nd, Sm, Eu, Tb–Lu) crystallise isotypically to $Gd_2[B_2(SO_4)_6]$ in space group *C*2/*c* with four formula units per unit cell (Fig. 2).[11] The cationic substructure (*d*(Eu–Eu) > 560 pm) shown in Fig. 3 comprises undulated ladder-shaped bands along [001] centred at (0, 0, *z*) and ($\frac{1}{2}$, $\frac{1}{2}$, *z*). In-between these bands, the complex anions $[B_2(SO_4)_6]^{6-}$ are arranged. The anion consists of a *vierer*-ring of alternating corner-sharing borate and sulfate tetrahedra. Each borate tetrahedron is furthermore saturated with two sulfate tetrahedra, thus maintaining the above mentioned supertetrahedral moiety – here present in an edge-sharing dimer. The deviation from tetrahedral symmetry[14] amounts to 0.33% for $BO_4$, and 0.07–0.19% for the different sulfate groups, thus all tetrahedra are pretty regular. Adopting the silicate nomenclature by Liebau, the anion can be described as open-branched *vierer* single ring {***oB***, 1*r*}$[B_2S_2O_{12}(SO_3)_4]^{6-}$ and hence be classified as cycloborosulfate (Fig. 5).[15] In nature, a similar backbone is found in the mineral *eakerite* ($Ca_2Al_2Sn[Si_6O_{18}](OH)_2{\cdot}2H_2O$), comprising the silicate anion {***oB***, 1*r*}$[Si_4O_{12}(SiO_3)_2]^{12-}$.[15,16] Unbranched *vierer* single rings are also present in other minerals like *verplanckite* ($Ba_{12}(Mn,Ti,Fe)_6[Si_4O_{12}]_3(O,OH)_2(OH,H_2O)_7Cl_9$)[17] and in silicates like $KHSiO_3$[18] as well as $K(UO)Si_2O_6$.[19] By eying the supertetrahedron $B(SO_4)_4$ itself as analogue to $SiO_4$, the anion thus pre-

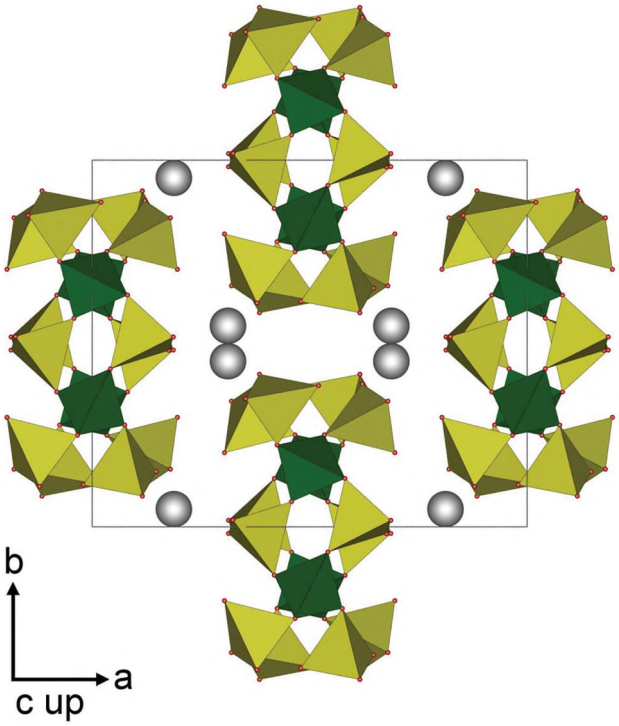


Fig. 2 Crystal structure of $Eu_2[B_2(SO_4)_6]$ along [00$\bar{1}$] (borate tetrahedra green, sulfate tetrahedra yellow, and europium cations grey).

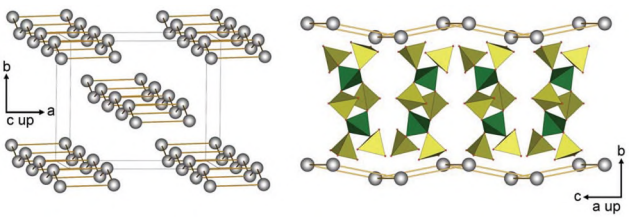


Fig. 3 Ladder-shaped bands of the cationic substructure along [00$\bar{1}$] (left) and arrangement of the anions between these bands (right); the orange lines do not represent bonds in a chemical sense but help in the understanding of the crystal structure.

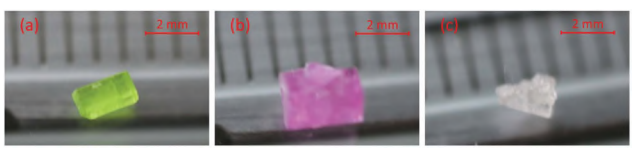


Fig. 1 Crystals of $Pr_2[B_2(SO_4)_6]$ (a), $Nd_2[B_2(SO_4)_6]$ (b), and $Eu_2[B_2(SO_4)_6]$ (c). The three crystals were synthesised from the rare earth metal chlorides.

sents an edge-sharing dimer comparable to a section of the chains in $SiS_2$.[20]

The cations occupy the Wyckoff site 8f with site symmetry 1 and are coordinated by two bidentate and four monodentate anions. Two coordinating oxygen atoms stem from bridging sulfate tetrahedra, and six oxygen atoms from terminal sulfate tetrahedra, resulting in a slightly distorted square antiprismatic coordination environment (Fig. 4). The Eu–O distances

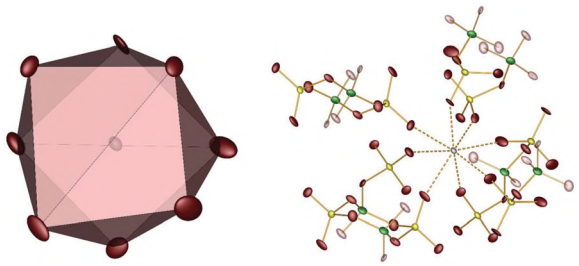

Fig. 4 Square antiprismatic coordination environment of $Eu^{3+}$ (left) and enlarged coordination sphere (right). Ellipsoids are set to 70% probability and further connected oxygen atoms are shown with transparency.

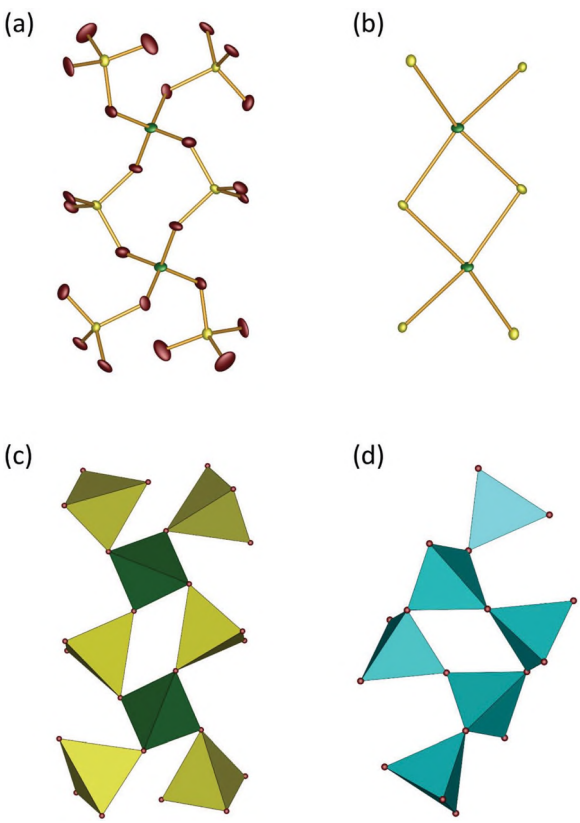


Fig. 5 (a) Ball-stick model of the anion {*oB*, 1*r*}$[B_2(SO_4)_6]^{6-}$ (ellipsoids are set to 70% probability), (b) an illustration of the edge-sharing super-tetrahedra formed by the boron and sulfur tetrahedral centres, (c) a representation of {*oB*, 1*r*}$[B_2(SO_4)_6]^{6-}$ with closed tetrahedra compared with the {*oB*, 1*r*}$[Si_4O_{12}(SiO_3)_2]^{12-}$ unit present in eakerite (silicate tetrahedra in blue) (d).[16]

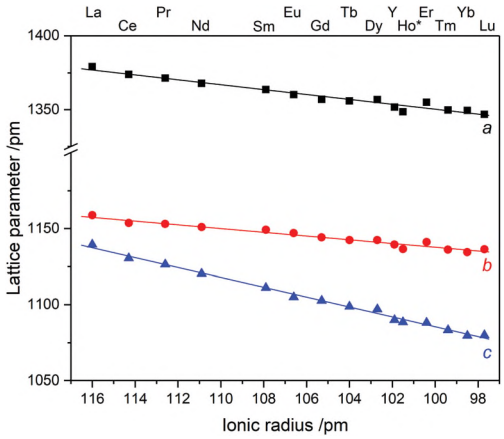


Fig. 6 Correlation of the ionic radii of the rare earth ions with the lattice parameters *a*, *b* and *c* of the title compounds measured at room temperature (*measured at 200 K, the estimated standard deviations of all values is smaller than the spot size).

Table 1 Selected interatomic distances (pm) and angles (°) in $Eu_2[B_2(SO_4)_6]$; the standard deviations are given in parentheses

| | |
|---|---|
| Eu–O | 228.8(5)–250.3(5) |
| $\Sigma r_{ion}$(Eu–O) | 244 |
| S–$O^{br.}$ | 151.4(5)–154.9(6) |
| S–$O^{term.}$ | 142.7(6)–146.0(5) |
| B–O | 143.7(10)–148.5(9) |
| O–S–O | 103.1(3)–114.5(3) |
| O–B–O | 105.7(6)–110.5(6) |

range from 229–250 pm (Table 1) and are close to the sum of the ionic radii ($\sum r_{ion}$ = 244 pm).[21]

As a result of the lanthanide contraction, the lattice parameters decrease smoothly within the isotypic series $RE_2[B_2(SO_4)_6]$ (*RE* = Y, La–Nd, Sm–Lu) as shown in Fig. 6. The slope along the *a* and *c* direction is slightly more pronounced, based on the previous mentioned ladder-shaped bands of the cations developing along the *a*–*c* plane. However, the monoclinic angle remains almost unaffected.

## Vibrational spectroscopy

The infrared spectrum in Fig. 7 (full spectrum and spectra of the other rare earth borosulfates in the ESI in Fig. S5†) displays bands in the region of 1400–400 $cm^{-1}$, which indicates the presence of boron and sulfur centred oxygen tetrahedra.[22] Based on previous calculations on borosulfates,[23] an assignment of bands can be suggested. The bands below 500 $cm^{-1}$ can be assigned to asymmetric bending vibrations $\delta_{asym}$(O–S–O). In the region of 720–500 $cm^{-1}$, asymmetric bending vibrations $\delta_{asym}$(O–S–O), $\delta_{asym}$(O–B–O), and bridging $\delta_{asym}$(B–O–S) occur. Symmetric stretching vibrations $\nu_{sym}$(S–O) and asymmetric bending vibrations $\delta_{asym}$(O–B–O) range from 950–850 $cm^{-1}$. Bands between 1060–950 $cm^{-1}$ are assigned to the symmetric and asymmetric stretching vibrations $\nu_{sym}$(B–O)

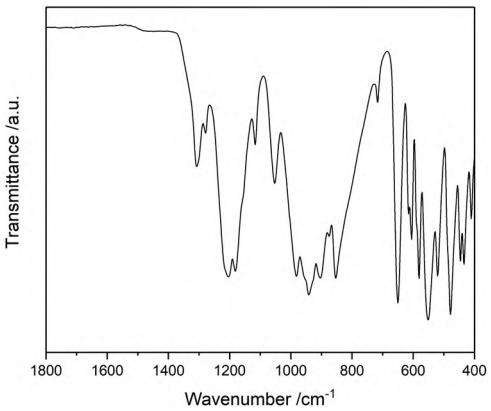


Fig. 7 Infrared spectrum of $Eu_2[B_2(SO_4)_6]$.

and $\nu_{asym}$(B–O) of the borate tetrahedra. At higher wavenumbers above 1100 $cm^{-1}$, the symmetric and asymmetric vibrations $\nu_{sym}$(S–O) and $\nu_{asym}$(S–O) are present, dominated by the vibrations of the terminal oxygen atom.

### Fluorescence spectroscopy

The fluorescence spectrum (Fig. 8) of $Ce_2[B_2(SO_4)_6]$ shows two emission bands at 300 and 318 nm, both lying in the deep UV region. They result from the parity and electric dipole allowed 5d → 4f transition and can be assigned to 5d → $^2F_{5/2}$ and 5d → $^2F_{7/2}$, respectively. The excitation spectrum reveals two distinct transitions from the ground state $^2F_{7/2}$ to the splitted 5d states peaking at 240 and 287 nm. This results in a remarkably small Stokes shift of 1510 $cm^{-1}$ as discussed below. Furthermore, a shoulder on the high energy end of the transition at 240 nm indicates further, weaker transitions, which is in accordance to the low site symmetry of the cation, *i.e.* 1.[24]

In comparison, $YF_3$:$Ce^{3+}$ [25] or YOCl:$Ce^{3+}$ [24] show emission wavelengths of 294 and 310 or 380 nm, respectively. Accordingly, the $[B_2(SO_4)_6]^{6-}$ anion also shows a weak covalency and a weak nephelauxetic effect; hence, the barycentre of the 5d levels is at comparably high energies.[26] This is in accordance with our previous findings on the coordination influence of borosulfate anions on outer transition metals.[13] Moreover, the observed Stokes shift of 1510 $cm^{-1}$ is even smaller than for $YF_3$:$Ce^{3+}$ (5200 $cm^{-1}$) and YOCl:$Ce^{3+}$ (5300 $cm^{-1}$), which might be explained by the higher rigidity of the borosulfate anions in comparison to the non-condensed halide or oxide anions.[3]

Upon doping $Y_2[B_2(SO_4)_6]$ with $Ce^{3+}$ a red-shift of the excitation and emission bands is observed in comparison to the pure compound (Fig. 8). Due to the different ionic radii of eightfold coordinated $Y^{3+}$ ($r_{ion}$ = 102 pm) and $Ce^{3+}$ ($r_{ion}$ = 114 pm), a stronger interaction with the ligands in the doped compound is expected. This increase in ligand field splitting results in a decrease of the energy difference between the 4f and 5d states and therefore in larger emission and excitation wavelengths.

$Eu_2[B_2(SO_4)_6]$ shows intense orange-red luminescence upon excitation. The emission bands can be assigned to $^5D_0$ → $^7F_J$ ($J$ = 0, 1, 2, 3, 4, 5) and $^5D_1$ → $^7F_5$ (Fig. 9).[27] The highest intensity in the emission spectrum is attributed to the hypersensitive transition $^5D_0$ → $^7F_2$ (615 nm), as $Eu^{3+}$ is located on the general Wyckoff site 8f with site symmetry 1. Hence, it shows a higher intensity than the magnetic dipole allowed transition $^5D_0$ → $^7F_1$. The transitions $^5D_0$ → $^7F_J$ ($J$ = 0, 3, 5) are very weak, as they violate the selection rule $|\Delta J|$ = 2, 4, 6, if $J$ = 0 for induced magnetic dipole transitions and $|J|$ = 0, ±1 for magnetic dipole transitions.[28] Furthermore, a splitting of the $^7F_1$ and $^7F_2$ states is clearly visible, based on the low site symmetry and a resulting break-up of the 2$J$ + 1 degenerated states.[28] Thus, the $^7F_0$ state remains as a single line and can be seen as a prove for just a single crystallographic site for $Eu^{3+}$. Beside the hypersensitive transition, the $^5D_0$ → $^7F_4$ transition also shows a strong intensity, which often occurs in square antiprismatic or slightly distorted square antiprismatic coordination environments.[28] This explains, why the hypersensitive transition $^5D_0$ → $^7F_2$ still has the highest intensity, but is not dominating the spectrum, as it would be expected for the site symmetry 1.

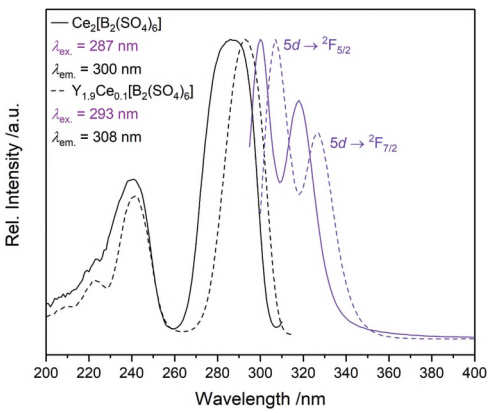


Fig. 8 Corrected excitation (black) and emission (violet) spectra of $Ce_2[B_2(SO_4)_6]$ (solid line) and $Y_{1.9}Ce_{0.1}[B_2(SO_4)_6]$ (dashed line).

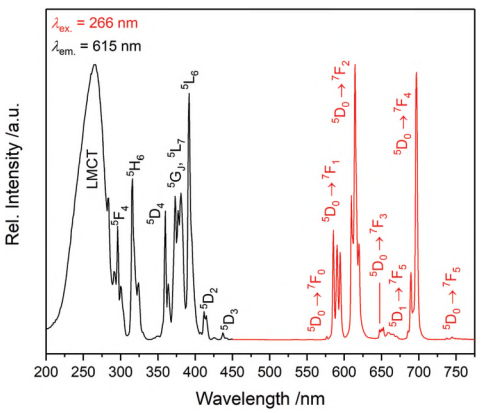


Fig. 9 Corrected excitation (black) and emission (red) spectra of $Eu_2[B_2(SO_4)_6]$ at room temperature.

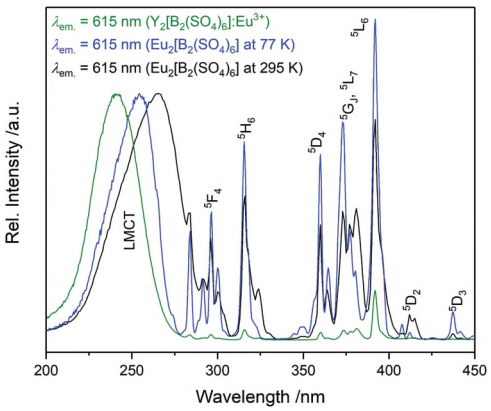


**Fig. 10** Comparison between the excitation spectra of $Y_2[B_2(SO_4)_6]$:$Eu^{3+}$ (green), $Eu_2[B_2(SO_4)_6]$ at 77 K (blue) and $Eu_2[B_2(SO_4)_6]$ at 295 K (black).

The excitation spectrum shows sharp transitions originating from the ground state $^7F_0$.[27] Furthermore, a broad ligand-to-metal-charge-transfer (LMCT) at 266 nm is present and is in the typical region for oxide coordinated europium compounds.[29] In Fig. 10, a comparison between the CT in $Eu^{3+}$ for different temperatures and for different site sizes is shown. A decrease of the wavelength of the CT transition from 266 nm for $Eu_2[B_2(SO_4)_6]$ at 295 K to 255 nm for $Eu_2[B_2(SO_4)_6]$ at 77 K to 241 nm for $Y_2[B_2(SO_4)_6]$ at 295 K is visible. This trend can be explained by the decreasing site size for $Eu^{3+}$ at 295 and 77 K as well as the smaller $Y^{3+}$ site. Thus a higher repulsion between the electrons of $Eu^{3+}$ and the electrons of the ligand lead to higher charge transfer energies.[30]

The excitation and emission spectra of $Y_{2-2x}Tb_{2x}[B_2(SO_4)_6]$ ($x$ = 0.001, 0.01, 0.05, 1) are shown in Fig. 11. The emission monitored at 365 nm originates from $^5D_3 \rightarrow {}^7F_J$ ($J$ = 5, 4, 3, 2) and $^5D_4 \rightarrow {}^7F_J$ ($J$ = 6, 5, 4, 3).[31] The strongest emission for all doping concentrations is the $^5D_4 \rightarrow {}^7F_5$ transition at 542 nm, as it has the highest probability for electric-dipole and magnetic-dipole induced transitions.[32] In the pure Tb compound, the emissions originating from the $^5D_3$ level are completely absent, due to cross-relaxation processes of neighbouring $Tb^{3+}$ ions:

$$^5D_3\ (Tb1^{3+}) + {}^7F_6\ (Tb2^{3+}) \rightarrow {}^5D_4\ (Tb1^{3+}) + {}^7F_0\ (Tb2^{3+}) \quad (1)$$

With decreasing $Tb^{3+}$ concentration, an average increase of the Tb–Tb distances occurs and the cross-relaxation is suppressed. Hence the integrated intensity ratio of the emissions $^5D_3 \rightarrow {}^7F_J$ to $^5D_4 \rightarrow {}^7F_J$ drastically increases from 0.05 to 0.001 doped sample (Fig. S8† in the ESI†).

The excitation spectrum shows several 4f → 4f transitions in the range of 260–400 nm originating from the ground state $^7F_6$ (Fig. S6 and Table S1 in the ESI†).[31] At higher energies, two parity allowed 4f → 5d transitions at 212 and 254 nm are visible. Similar values were previously reported for $YF_3$:$Tb^{3+}$ (215, 255 nm)[25] and are in the typical region for rather weakly coordinated $Tb^{3+}$ compounds.[33] The transition within $Tb^{3+}$ to the lowest 5d state is spin forbidden leading to a relatively sharp band with a FWHM of approximately 1250 $cm^{-1}$. This is in good accordance to the 4f → 5d transition in $CaF_2$:$Tb^{3+}$.[34]

## Magnetic properties

The magnetic susceptibility $\chi$ of $Eu_2[B_2(SO_4)_6]$ measured in dependence of temperature is depicted in Fig. 12. At 300 K, the susceptibility per Eu atom is $\chi_{mol}$ = 7.76(1)×$10^{-3}$ emu $mol^{-1}$, leading to an experimental magnetic moment of $\mu_{eff}$ = 3.05(1)$\mu_B$ calculated *via*:

$$\mu_{eff} = \sqrt{\frac{3k_B}{\mu_0 N_A {\mu_B}^2} T\chi_{mol}} \approx \sqrt{8\chi_{mol}T}$$

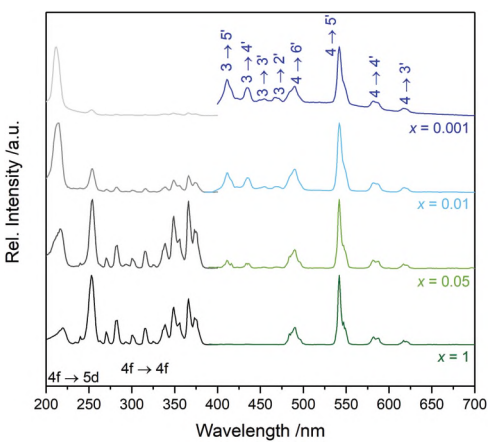


**Fig. 11** Excitation ($\lambda_{em.}$ = 542 nm) and emission ($\lambda_{ex.}$ = 365 nm) spectra of $Y_{2-2x}Tb_{2x}[B_2(SO_4)_6]$ with $x$ = 0.001 (light grey and dark blue) $x$ = 0.01 (grey and light blue), $x$ = 0.05 (dark grey and light green), and $x$ = 1 (black and dark green); the assignments of the excitation bands can be found in Table S1;† the assignment of the emission bands corresponds to $^5D_J \rightarrow {}^7F_J$.

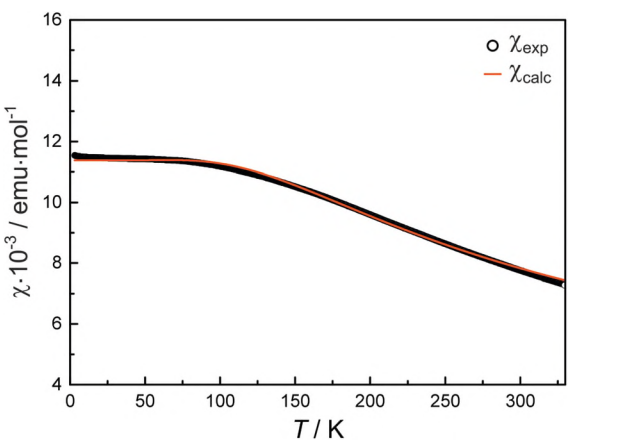


**Fig. 12** Temperature dependence of the magnetic susceptibility of $Eu_2[B_2(SO_4)_6]$ measured with a magnetic flux density of 10 kOe. The calculated susceptibility was obtained by fitting the experimental data with the van Vleck expression for paramagnetic susceptibilities of free $Eu^{3+}$ cations.

with the Boltzmann constant $k_B$, the Avogadro constant $N_A$ and the Bohr magneton $\mu_B$. The course of the susceptibility indicates typical van Vleck paramagnetic behaviour of trivalent europium species. The $^7F_J$ multiplet of the $Eu^{3+}$ ion consists of seven states. The $^7F_0$ ground state is only relevant for the temperature variation of the magnetic properties if the separation of the multiplet components is large compared with $k_BT$. For the commensurable case, the contribution of different components has to be included. The paramagnetic susceptibility can be written by the following expression based on van Vlecks theory of electric and magnetic susceptibilities:[35]

$$\chi_{para} = \frac{N_A {\mu_B}^2}{Z}\frac{A}{3\lambda}$$

with the respected energy states considered by the terms $A$ and $Z$, which were formulated by Nagata and co-workers.[36] The coupling parameter $\lambda$ is the only variable term and can be determined by fitting the experimental data with the given expression. A high value of $\lambda$ indicates a low hybridisation from the ground state to the excited state. The value of the temperature independent susceptibility also decreases with an increasing coupling parameter. The susceptibility remains almost constant underneath about 85 K at a value of $11.44(1) \times 10^{-3}$ emu $mol^{-1}$. The plateau at low temperatures is caused by the exclusive population of the $^7F_0$ ground state with no contribution to the susceptibility. The fitted coupling constant of $\lambda$ = 589 K is well above the one reported for $EuBO_3$ ($\lambda$ = 471 K),[36] which furthermore confirms the weak coordination behaviour of the anions.

The temperature dependence of the magnetic moment is depicted in Fig. S8.† The effective magnetic moment of the pyrochlore type compound $Eu_2Ta_2O_6N$[37] was added for comparison. The course of both compounds is in line with previously characterized $Eu^{3+}$ containing compounds.[39]

### $^{151}$Eu Mößbauer spectroscopy

In addition to the magnetic measurements, a $^{151}$Eu Mößbauer spectrum of $Eu_2[B_2(SO_4)_6]$ was recorded (Fig. 13). In agreement with the crystal structure, the spectrum could be well reproduced by a single signal with an isomer shift of $\delta$ = 0.047(9) mm $s^{-1}$ and a quadrupole splitting of $\Delta E_Q$ = −3.70(8) mm $s^{-1}$. The isomer shift is in the usual range for trivalent Eu species[38] and therefore in line with the expected oxidation state ($Eu_2^{+III}B_2^{+III}S_6^{+VI}O_{24}^{-II}$). Similar shifts are reported for $Eu_2(SO_4)_3$ ($\delta$ = −0.01 mm $s^{-1}$ *vs.* $Eu_2O_3$) and $Eu_2(SO_4)_3{\cdot}8H_2O$ ($\delta$ = 0.22 mm $s^{-1}$).[40] The quadrupole splitting of $\Delta E_Q$ = −3.70 mm $s^{-1}$ is caused by the non-cubic site symmetry of the Eu site. The experimental line width of $\Gamma$ = 2.90(5) mm $s^{-1}$ is in the usual range.

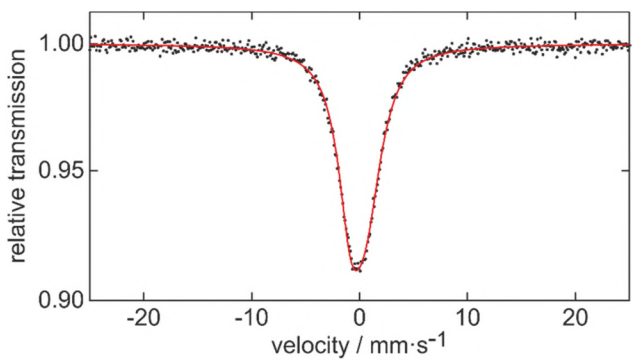


**Fig. 13** Experimental and simulated $^{151}$Eu Mößbauer spectrum of $Eu_2[B_2(SO_4)_6]$ at 78 K.

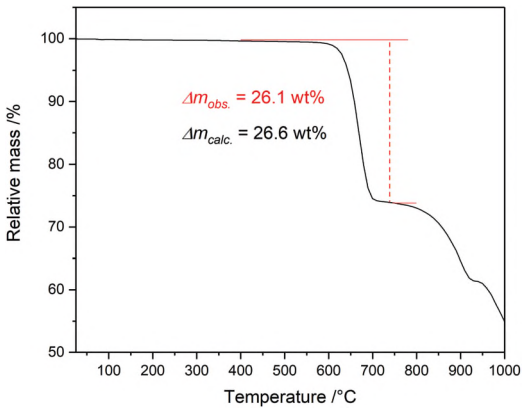


**Fig. 14** Thermogram of $Eu_2[B_2(SO_4)_6]$ recorded up to 1000 °C in nitrogen atmosphere.

### Thermal analysis

The thermal stability of $Eu_2[B_2(SO_4)_6]$ was measured up to 1000 °C under nitrogen atmosphere (Fig. 14). For convenience reasons we use in this section degrees centigrade instead of the Kelvin scale. The decomposition starts at around 570 °C according to the following reaction scheme:

$$Eu_2[B_2(SO_4)_6] \rightarrow Eu_2(SO_4)_3 + B_2O_3 + 3SO_2\ (g) + 1.5O_2(g)$$

The theoretical mass loss of 26.6 wt% corresponding to 3 mol $SO_3$ – presumably decomposing to $SO_2$ and $O_2$ under these conditions – is in good accordance to the observed one of 26.1 wt%. Similar decomposition schemes were recently observed for further borosulfates as well.[11,13] The subsequent mass losses suggest the decomposition of $Eu_2(SO_4)_3$ to $Eu_2O_3$ (Fig. S9 in the ESI†),[41] which apparently reacts with $B_2O_3$ to form $EuBO_3$ as proven by PXRD (Fig. S10†).[42]

A comparison of the hitherto reported thermal stabilities of borosulfates is given in Table 2. Several trends can be deduced from these results. Firstly, directly connected sulfate tetrahedra as present in $Li[B(S_2O_7)_2]$[9] lead to very weak thermal stabilities, as expected by the violation of Paulings electrostatic valence rule.[43] Secondly, the thermal stability is higher for lower condensed networks ($Na_5[B(SO_4)_4]$,[9] $Mg_4[B_2O(SO_4)_6]$[13]) in comparison to higher condensed ones ($K_3[B(SO_4)_3]$[9] and $Ba[B_2O(SO_4)_3]$[11]). Thirdly, higher charges on the cationic site and thus, higher electrostatic interactions within the compounds also increase the thermal stability of borosulfates. Hence, $Eu_2[B_2(SO_4)_6]$ with trivalent europium and a low condensed

Table 2 Comparison of the thermal stabilities of hitherto reported borosulfates

| Compound | $T_{decomp.}$/°C | Ref. |
|---|---|---|
| $Li[B(S_2O_7)_2]$ | 77 | 9 |
| $K_3[B(SO_4)_3]$ | 396 | 9 |
| $Na_5[B(SO_4)_4]$ | 434 | 9 |
| $Ba[B_2O(SO_4)_3]$ | 480 | 11 |
| $Mg_4[B_2O(SO_4)_6]$ | 500 | 13 |
| $Eu_2[B_2(SO_4)_6]$ | 570 | This work |

$[B_2(SO_4)_6]^{6-}$ anion leads to the highest thermal stability for borosulfates observed so far.

# Experimental section

### Synthesis

***RE*$_2$[B$_2$(SO$_4$)$_6$].** The superacid $H_5[B(SO_4)_4]$ was synthesised in a Schlenk flask by dissolving $B(OH)_3$ (185.5 mg, 3 mmol) in 2.5 mL $H_2SO_4$. The flask was flushed with $N_2$ and heated to 200 °C for 1 h and afterwards cooled down to 120 °C. Subsequently, 0.3 mL oleum (65%) were added.[13] For a typical synthesis, 2 mmol with respect to the rare earth ion of the freshly dehydrated metal chloride (Pr, Nd, Eu), metal oxide ($La_2O_3$, $CeO_2$, $Sm_2O_3$, $Tb_4O_7$, $Dy_2O_3$, $Er_2O_3$, $Tm_2O_3$, $Lu_2O_3$), or metal powders (Ho, Yb) were added and the suspension was stirred for 10 min. In case of doped borosulfates, the respective metal oxides were ground together before adding to the acid. The resulting suspension was transferred into a silica glass ampoule (outer diameter: 1.2 cm, wall thickness: 0.1 cm) and fused. The ampoule was placed in a muffle furnace applying the following temperature program: heating to 300 °C with 100 °C h$^{-1}$, holding the temperature for 120 h, and cooling down to room temperature with 50 °C h$^{-1}$.

Several single-crystals were formed in the acid. The ampoules were opened after cooling down with liquid nitrogen. The bulk excess of the acid was pipetted, whereas the adhesive acid was evaporated at 300 °C. The crystals are sensitive towards moisture and hence were stored under inert conditions.

### Crystal structure determination

Immediately after opening the ampule, single-crystals were transferred into perfluorinated polyether and selected for single-crystal XRD. Diffraction data for all compounds were collected with a Bruker D8 Venture diffractometer using Mo-$K_\alpha$ radiation ($\lambda$ = 0.71073 Å). The absorption correction was done with the multi-scan method, then the crystal structures were solved with direct methods and refined by the full-matrix least-squares technique within the SHELXTL program.[44]

Further details of the crystal structure determination are listed in Tables 3 and 4 as well as in the ESI in Tables S2 and S3.† Further details of the crystal structures investigations may be obtained from the Fachinformationszentrum Karlsruhe, 76344 Eggenstein-Leopoldshafen, Germany (Fax: +49-7247-808-666; E-Mail: crysdata@fizkarlsruhe.de, http://www.fiz-karlsruhe.de/requestfordepositeddata.html) on quoting the depository numbers $Eu_2[B_2(SO_4)_6]$ (CSD 1894174), $Ce_2[B_2(SO_4)_6]$ (CSD 1894175), $La_2[B_2(SO_4)_6]$ (CSD 1894176), $Ho_2[B_2(SO_4)_6]$ (CSD 1894177), $Lu_2[B_2(SO_4)_6]$ (CSD 1894178), $Dy_2[B_2(SO_4)_6]$ (CSD 1894179), $Pr_2[B_2(SO_4)_6]$ (CSD 1894180), $Er_2[B_2(SO_4)_6]$ (CSD 1894181), $Nd_2[B_2(SO_4)_6]$ (CSD 1894182), $Tb_2[B_2(SO_4)_6]$ (CSD 1894183), $Tm_2[B_2(SO_4)_6]$ (CSD 1894184), $Y_2[B_2(SO_4)_6]$ (CSD 1894185), $Yb_2[B_2(SO_4)_6]$ (CSD 1894186) and $Sm_2[B_2(SO_4)_6]$ (CSD 1894187 and CSD 433354).†

### X-ray powder diffraction

The samples were ground and filled into a Hilgenberg glass capillary (outer diameter 0.3 mm, wall thickness 0.01 mm) inside a glovebox. The data were collected with a Bruker D8 Advance diffractometer with Cu-$K_\alpha$ radiation ($\lambda$ = 1.54184 Å) with a 1D LynxEye detector.

The residue of the sample after the thermal analysis was measured with a Seifert 3003 TT diffractometer with Cu-$K_\alpha$ radiation ($\lambda$ = 1.54184 Å) with a 1D line detector.

### Infrared spectroscopy

The infrared spectra were recorded using a Bruker EQUINOX 55 FT-IR spectrometer equipped with a platinum ATR setup in a range of 4000–400 cm$^{-1}$.

### Fluorescence spectroscopy

Solid-state excitation and emission spectra were recorded at room temperature using a Horiba FluoroMax-4 fluorescence spectrometer equipped with a xenon discharge lamp scanning a range from 200 to 800 nm. The excitation spectra were corrected with respect to the lamp intensity. Low temperature measurements were performed with a liquid nitrogen dewar assembly within the same device.

### Optical spectroscopy

The optical reflection spectra of $Nd_2[B_2(SO_4)_6]$ (Fig. S11†) and $Er_2[B_2(SO_4)_6]$ (Fig. S12†) were measured with a Varian Cary 300 Scan UV/Vis spectrophotometer in the range of 200–800 nm.

### Magnetic property measurements

The Vibrating Sample Magnetometer (VSM) of the Quantum Design Physical Property Measurement System (PPMS) was used for the magnetic characterization of $Eu_2[B_2(SO_4)_6]$. A polypropylene capsule was filled with 28.369 mg of the powdered sample and attached to the sample holder rod. The sample was investigated in the temperature range of 3–330 K with an applied magnetic field of 10 kOe.

### $^{151}$Eu Mößbauer spectroscopy

For the $^{151}$Eu Mößbauer spectroscopic measurement of $Eu_2[B_2(SO_4)_6]$, the 21.53 keV transition of $^{151}$Eu of a $^{151}$Sm:$EuF_3$ source with an activity of 130 MBq was used (2% of the total activity). The sample was prepared in a thin-walled PMMA container (2 cm diameter) with an optimized thickness according to Long *et al.*[45] The measurement was conducted in

**Table 3** Crystal data and details of the structure refinements for $RE_2[B_2(SO_4)_6]$ with *RE* = Y, La–Nd, Sm, Eu; the standard deviations are given in parentheses

| | $Y_2[B_2(SO_4)_6]$ | $La_2[B_2(SO_4)_6]$ | $Ce_2[B_2(SO_4)_6]$ | $Pr_2[B_2(SO_4)_6]$ | $Nd_2[B_2(SO_4)_6]$ | $Sm_2[B_2(SO_4)_6]$ | $Eu_2[B_2(SO_4)_6]$ |
|---|---|---|---|---|---|---|---|
| Temperature/K | 287(2) | 298(2) | 298(2) | 300(2) | 299(2) | 298(2) | 300(2) |
| Molar weight/g mol$^{-1}$ | 775.80 | 875.80 | 878.22 | 879.80 | 886.46 | 898.68 | 901.90 |
| Crystal system | Monoclinic | Monoclinic | Monoclinic | Monoclinic | Monoclinic | Monoclinic | Monoclinic |
| Space group | *C*2/*c* | *C*2/*c* | *C*2/*c* | *C*2/*c* | *C*2/*c* | *C*2/*c* | *C*2/*c* |
| Crystal shape | Block | Block | Block | Block | Block | Block | Block |
| Colour | Colourless | Colourless | Yellow | Green | Violet | Colourless | Colourless |
| *a*/pm | 1351.72(5) | 1379.24(17) | 1374.00(5) | 1371.14(11) | 1367.75(4) | 1363.3(3) | 1360.2(6) |
| *b*/pm | 1139.41(4) | 1158.87(14) | 1153.71(4) | 1153.05(9) | 1151.34(4) | 1149.2(3) | 1147.0(5) |
| *c*/pm | 1089.94(4) | 1139.54(14) | 1130.57(4) | 1126.43(9) | 1120.46(3) | 1111.2(2) | 1105.0(5) |
| *β*/° | 93.4470(10) | 93.611(4) | 93.6606(12) | 93.638(2) | 93.5909(8) | 93.567(6) | 93.465(9) |
| Volume/10$^6$ pm$^3$ | 1675.65(11) | 1817.8(4) | 1788.52(11) | 1777.6(2) | 1760.97(9) | 1738.0(7) | 1720.8(12) |
| *Z* | 4 | 4 | 4 | 4 | 4 | 4 | 4 |
| Calculated density $D_x$/g cm$^{-3}$ | 3.08 | 3.20 | 3.26 | 3.29 | 3.34 | 3.44 | 3.48 |
| Absorption coefficient $\mu$/mm$^{-1}$ | 7.8 | 5.5 | 5.9 | 6.3 | 6.7 | 7.5 | 8.1 |
| *F*(000) | 1504 | 1648 | 1656 | 1664 | 1672 | 1688 | 1696 |
| Radiation ($\lambda$/Å) | 0.71073 | 0.71073 | 0.71073 | 0.71073 | 0.71073 | 0.71073 | 0.71073 |
| Diffractometer | Bruker D8 Venture | Bruker D8 Venture | Bruker D8 Venture | Bruker D8 Venture | Bruker D8 Venture | Bruker D8 Venture | Bruker D8 Venture |
| Absorption correction | Multi-scan | Multi-scan | Multi-scan | Multi-scan | Multi-scan | Multi-scan | Multi-scan |
| Transmission factor (min./max.) | 0.6247/0.7489 | 0.6525/0.7477 | 0.6730/0.7455 | 0.6174/0.7461 | 0.6359/0.7490 | 0.6730/0.7479 | 0.5053/0.7459 |
| Index range $h\|k\|l$ (min./max.) | −22/23\|−19/19\|−18/18 | −24/24\|−20/20\|−20/19 | −17/17\|−14/14\|−14/14 | −19/19\|−16/15\|−16/16 | −27/27\|−23/23\|−22/22 | −19/19\|−16/16\|−15/15 | −17/17\|−14/14\|−14/14 |
| Theta range/° | 2.340 < $\theta$ < 37.500 | 2.297 < $\theta$ < 39.074 | 2.307 < $\theta$ < 27.444 | 2.310 < $\theta$ < 30.555 | 2.314 < $\theta$ < 45.670 | 2.320 < $\theta$ < 29.998 | 2.32 < $\theta$ < 27.49 |
| Reflections collected | 30 731 | 35 142 | 16 577 | 24 061 | 50 621 | 19 598 | 6047 |
| Independent reflections | 4423 | 5292 | 2039 | 2719 | 7512 | 2543 | 1968 |
| Observed reflections ($I > 2\sigma$) | 3942 | 4258 | 1745 | 2565 | 6470 | 2305 | 1541 |
| $R_{int}$ | 0.0426 | 0.0633 | 0.0630 | 0.0247 | 0.0473 | 0.0369 | 0.0670 |
| Refined parameters | 155 | 155 | 154 | 155 | 155 | 155 | 148 |
| $R_1$ (all data) | 0.0290 | 0.0461 | 0.0307 | 0.0160 | 0.0338 | 0.0205 | 0.0638 |
| w$R_2$ (all data) | 0.0493 | 0.0543 | 0.0453 | 0.0343 | 0.0455 | 0.0370 | 0.0784 |
| GooF | 0.994 | 1.031 | 1.044 | 1.109 | 1.040 | 1.002 | 1.051 |
| Residual electron density (min./max.)/e$^-$ Å$^{-3}$ | −0.53/0.68 | −1.08/1.09 | −0.66/0.62 | −0.54/0.58 | −1.35/1.59 | −0.63/0.59 | −1.75/1.64 |

**Table 4** Crystal data and details of the structure refinements for $RE_2[B_2(SO_4)_6]$ with *RE* = Tb–Lu; the standard deviations are given in parentheses

| | $Tb_2[B_2(SO_4)_6]$ | $Dy_2[B_2(SO_4)_6]$ | $Ho_2[B_2(SO_4)_6]$ | $Er_2[B_2(SO_4)_6]$ | $Tm_2[B_2(SO_4)_6]$ | $Yb_2[B_2(SO_4)_6]$ | $Lu_2[B_2(SO_4)_6]$ |
|---|---|---|---|---|---|---|---|
| Temperature/K | 298(2) | 301(2) | 200(2) | 300(2) | 299(2) | 300(2) | 300(2) |
| Molar weight/g mol$^{-1}$ | 915.82 | 922.98 | 927.84 | 932.50 | 935.84 | 944.06 | 947.92 |
| Crystal system | Monoclinic | Monoclinic | Monoclinic | Monoclinic | Monoclinic | Monoclinic | Monoclinic |
| Space group | *C*2/*c* | *C*2/*c* | *C*2/*c* | *C*2/*c* | *C*2/*c* | *C*2/*c* | *C*2/*c* |
| Crystal shape | Block | Block | Block | Block | Block | Block | Block |
| Colour | Colourless | Colourless | Pale-yellow | Colourless | Colourless | Colourless | Colourless |
| *a*/pm | 1356.01(6) | 1356.83(19) | 1350.53(14) | 1355.1(5) | 1349.81(4) | 1349.49(11) | 1346.9(3) |
| *b*/pm | 1142.48(5) | 1142.48(16) | 1140.95(11) | 1141.1(4) | 1136.17(3) | 1134.52(9) | 1136.4(3) |
| *c*/pm | 1098.81(5) | 1097.03(17) | 1092.10(11) | 1088.2(4) | 1083.27(3) | 1079.61(9) | 1079.9(3) |
| $\beta$/° | 93.5342(13) | 93.450(4) | 93.453(3) | 93.410(12) | 93.4500(9) | 93.390(2) | 93.369(8) |
| Volume/$10^6$ pm$^3$ | 1699.05(13) | 1697.5(4) | 1679.7(3) | 1679.8(11) | 1658.31(8) | 1650.0(2) | 1650.2(7) |
| *Z* | 4 | 4 | 4 | 4 | 4 | 4 | 4 |
| Calculated density $D_x$/g cm$^{-3}$ | 3.58 | 3.61 | 3.67 | 3.69 | 3.75 | 3.80 | 3.82 |
| Absorption coefficient $\mu$/mm$^{-1}$ | 9.1 | 9.6 | 10.2 | 10.8 | 11.5 | 12.2 | 12.8 |
| *F*(000) | 1712 | 1720 | 1728 | 1736 | 1744 | 1752 | 1760 |
| Radiation ($\lambda$/Å) | 0.71073 | 0.71073 | 0.71073 | 0.71073 | 0.71073 | 0.71073 | 0.71073 |
| Diffractometer | Bruker D8 Venture | Bruker D8 Venture | Bruker D8 Venture | Bruker D8 Venture | Bruker D8 Venture | Bruker D8 Venture | Bruker D8 Venture |
| Absorption correction | Multi-scan | Multi-scan | Multi-scan | Multi-scan | Multi-scan | Multi-scan | Multi-scan |
| Transmission factor (min./max.) | 0.6547/0.7490 | 0.6663/0.7475 | 0.6038/0.7490 | 0.5827/7490 | 0.6035/0.7482 | 0.6527/0.7490 | |
| Index range $h\|k\|l$ (min./max.) | −26/26\|−22/22\|−22/21 | −21/21\|−18/18\|−17/17 | −18/18\|−16/16\|−15/15 | −21/21\|−18/18\|−17/17 | −18/18\|−15/15\|−15/15 | −18/18\|−15/15\|−15/15 | −20/20\|−17/17\|−16/16 |
| Theta range/° | $2.333 < \theta < 45.673$ | $2.332 < \theta < 34.992$ | $2.339 < \theta < 29.994$ | $2.335 < \theta < 34.996$ | $2.345 < \theta < 29.991$ | $2.347 < \theta < 29.999$ | $2.347 < \theta < 33.550$ |
| Reflections collected | 43 272 | 30 108 | 19 064 | 30 081 | 18 788 | 19 093 | 29 911 |
| Independent reflections | 7237 | 3745 | 2456 | 3711 | 2419 | 2409 | 3251 |
| Observed reflections ($I > 2\sigma$) | 6013 | 3132 | 2325 | 3342 | 2207 | 2238 | 2789 |
| $R_{int}$ | 0.0463 | 0.0689 | 0.0276 | 0.0423 | 0.0336 | 0.0289 | 0.0937 |
| Refined parameters | 155 | 154 | 155 | 155 | 155 | 155 | 155 |
| $R_1$ (all data) | 0.0395 | 0.0336 | 0.0142 | 0.0223 | 0.0179 | 0.0156 | 0.0333 |
| w$R_2$ (all data) | 0.0406 | 0.0453 | 0.0293 | 0.0388 | 0.0303 | 0.0281 | 0.0544 |
| GooF | 1.026 | 1.040 | 0.952 | 1.089 | 1.043 | 1.056 | 1.031 |
| Residual electron density (min./max.)/e$^-$ Å$^{-3}$ | −1.09/1.60 | −0.81/1.09 | −0.51/0.68 | −0.83/0.96 | −0.52/0.53 | −0.55/0.54 | −1.26/1.53 |

usual transmission geometry in a commercial bad cryostat at 78 K while the source was kept at room temperature. The program WinNormos for Igor was used to fit the spectrum.[46]

### Thermal analysis

The thermogravimetric analysis was done in alumina crucibles employing a NETZSCH STA 409 PC Luxx in nitrogen atmosphere and a heating ramp of 10 °C $min^{-1}$.

## Conclusions

Within this contribution, we presented the crystal structures of the rare earth borosulfates $RE_2[B_2(SO_4)_6]$ with *RE* = Y, La-Nd, Sm, Eu, Tb–Lu. The structures comprises an open-branched *vierer* single ring {***oB***, 1*r*}$[B_2S_2O_{12}(SO_3)_4]^{6-}$, similar to the silicate backbone in the mineral eakerite ($Ca_2Al_2Sn[Si_6O_{18}](OH)_2{\cdot}2H_2O$). Thus, the presented borosulfates can be classified as silicate analogous. Due to the presence of optically active rare earth ions, it was possible to measure luminescence spectra for borosulfates for the very first time. The excitation and emission spectra of $Ce^{3+}$, $Eu^{3+}$ and $Tb^{3+}$ revealed both, consistence of the optical properties with respect to the crystal structure and a weak coordination behaviour of the borosulfate ligands. This is in accordance to our previous contribution on the optical properties of transition metal borosulfates. Furthermore, the thermal stability was investigated and compared within the borosulfate family. Accordingly, low condensed anionic networks and high charges of the cations have the most impact on the thermal stability and hence $Eu_2[B_2(SO_4)_6]$ has the highest thermal stability for borosulfates so far.

Based on these results an investigation of divalent $Eu^{2+}$ ions in a borosulfate host, *e.g.* $Ba[B_2O(SO_4)_3]$[11] or $Sr[B_2O(SO_4)_3]$[47] is of great interest, in order to see whether this host is as weakly coordinating as the recently published $Ba[B_4O_6F_2]$, where even a 4f–4f-transition of the doped $Eu^{2+}$ ion was observed.[48]

## Conflicts of interest

There are no conflicts to declare.

## Acknowledgements

The authors thank the *Deutsche Forschungsgemeinschaft* (DFG) for financial support under the project HO 4503/5-1. Philip Netzsch thanks the Fonds der Chemischen Industrie (FCI) for a Ph. D. fellowship. Jörn Bruns is thankful for a research stipend (BR5269/1) donated by the *Deutsche Forschungsgemeinschaft.*

## Notes and references

1 (*a*) T. Jüstel, H. Nikol and C. Ronda, *Angew. Chem.*, 1998, **110**, 3250–3271; (*b*) H. A. Höppe, *Angew. Chem., Int. Ed.*, 2009, **48**, 3572–3582, (*Angew. Chem.*, 2009, **121**, 3626–3636); (*c*) Y.-C. Lin, M. Karlsson and M. Bettinelli, *Top. Curr. Chem.*, 2016, **374**, 21.

2 M. Sato, S. W. Kim, Y. Shimomura, T. Hasegawa, K. Toda and G. Adachi, *Handbook on the physics and chemistry of rare earths*, 2016, vol. 49, pp. 1–128.

3 R.-J. Xie and N. Hirosaki, *Sci. Technol. Adv. Mater.*, 2007, **8**, 588–600.

4 R. Mueller-Mach, G. Mueller, M. R. Krames, H. A. Höppe, F. Stadler, W. Schnick, T. Jüstel and P. Schmidt, *Phys. Status Solidi A*, 2005, **202**, 1727–1732.

5 R.-J. Xie, N. Hirosaki, K. Sakuma, Y. Yamamoto and M. Mitomo, *Appl. Phys. Lett.*, 2004, **84**, 5404–5406.

6 M. Zhang, J. Wang, W. Ding, Q. Zhang and Q. Su, *Appl. Phys. B*, 2007, **86**, 647–651.

7 H. A. Höppe, K. Kazmierczak, M. Daub, K. Förg, F. Fuchs and H. Hillebrecht, *Angew. Chem., Int. Ed.*, 2012, **51**, 6255–6257, (*Angew. Chem.*, 2012, **124**, 6359–6362).

8 L. Pauling, *Z. Kristallogr.*, 1933, **84**, 442–452.

9 M. Daub, K. Kazmierczak, P. Gross, H. Höppe and H. Hillebrecht, *Inorg. Chem.*, 2013, **52**, 6011–6020.

10 R. Kniep, G. Gözel, B. Eisenmann, C. Röhr, M. Asbrand and M. Kizilyalli, *Angew. Chem., Int. Ed. Engl.*, 1994, **33**, 749–751.

11 P. Gross, A. Kirchhain and H. A. Höppe, *Angew. Chem., Int. Ed.*, 2016, **55**, 4353–4355, (*Angew. Chem.*, 2016, **128**, 4426–4428).

12 W.-W. Wang, X. Xu, J.-T. Kong and J.-G. Mao, *Inorg. Chem.*, 2018, **57**, 163–174.

13 P. Netzsch, P. Gross, H. Takahashi and H. A. Höppe, *Inorg. Chem.*, 2018, **57**, 8530–8539.

14 (*a*) T. Balić Žunić and E. Makovicky, *Acta Crystallogr., Sect. B: Struct. Sci.*, 1996, **52**, 78–81; (*b*) E. Makovicky and T. Balić-Žunić, *Acta Crystallogr., Sect. B: Struct. Sci.*, 1998, **54**, 766–773.

15 F. Liebau, *Structural Chemistry of Silicates*, Springer, Heidelberg, 1985.

16 A. A. Kossiakoff and P. B. Leavens, *Am. Mineral.*, 1976, **61**, 956–962.

17 A. R. Kampf, A. A. Khan and W. H. Baur, *Acta Crystallogr., Sect. B: Struct. Crystallogr. Cryst. Chem.*, 1973, **29**, 2019–2021.

18 L. S. Dent Glasser, R. A. Howie and Y. Xi, *Z. Kristallogr.*, 1984, **168**, 307–312.

19 C.-S. Chen, S.-F. Lee and K.-H. Lii, *J. Am. Chem. Soc.*, 2005, **127**, 12208–12209.

20 J. Peters and B. Krebs, *Acta Crystallogr., Sect. B: Struct. Crystallogr. Cryst. Chem.*, 1982, **38**, 1270–1272.

21 R. D. Shannon, *Acta Crystallogr., Sect. A: Cryst. Phys., Diffr., Theor. Gen. Crystallogr.*, 1976, **32**, 751–767.

22 K. Nakamoto, *Infrared and Raman spectra of inorganic and coordination compounds. Part A: Theory and applications in inorganic chemistry*, Wiley, Hoboken, N.J, 6th edn., 2009.

23 (*a*) J. Bruns, M. Podewitz, M. Schauperl, B. Joachim, K. R. Liedl and H. Huppertz, *Chem. – Eur. J.*, 2017, **23**, 16773–16781; (*b*) J. Bruns, M. Podewitz, M. Schauperl, K. R. Liedl, O. Janka, R. Pöttgen and H. Huppertz, *Eur. J. Inorg. Chem.*, 2017, 3981–3989.

24 G. Blasse and A. Bril, *J. Chem. Phys.*, 1967, **47**, 5139–5145.
25 C. Peng, C. Li, G. Li, S. Li and J. Lin, *Dalton Trans.*, 2012, **41**, 8660–8668.
26 J. W. H. van Krevel, H. T. Hintzen, R. Metselaar and A. Meijerink, *J. Alloys Compd.*, 1998, **268**, 272–277.
27 W. T. Carnall, P. R. Fields and K. Rajnak, *J. Chem. Phys.*, 1968, **49**, 4450–4455.
28 K. Binnemans, *Coord. Chem. Rev.*, 2015, **295**, 1–45.
29 G. Blasse, *J. Solid State Chem.*, 1972, **4**, 52–54.
30 P. Dorenbos, *J. Lumin.*, 2005, **111**, 89–104.
31 W. T. Carnall, P. R. Fields and K. Rajnak, *J. Chem. Phys.*, 1968, **49**, 4447–4449.
32 T. Kano, in *Phosphor handbook*, ed. H. Yamamoto, S. Shionoya and W. M. Yen, CRC Press, Boca Raton, FL, London, 2nd edn., 2007.
33 P. Dorenbos, *J. Phys.: Condens. Matter*, 2003, **15**, 6249–6268.
34 E. Loh, *Phys. Rev.*, 1966, **147**, 332–335.
35 J. H. van Vleck, *The theory of Electric and Magnetic Susceptibilities*, Oxford University Press, 1932.
36 Y. Takikawa, S. Ebisu and S. Nagata, *J. Phys. Chem. Solids*, 2010, **71**, 1592–1598.
37 B. Anke, S. Hund, C. Lorent, O. Janka, T. Block, R. Pöttgen and M. Lerch, *Z. Anorg. Allg. Chem.*, 2017, **643**, 1824–1830.
38 G. K. Shenoy and F. E. Wagner, *Mössbauer isomer shifts*, North-Holland Publishing, Amsterdam, 1978.
39 A. Bronova, N. Kannengießer and R. Glaum, *Inorg. Chem.*, 2017, **56**, 9235–9246.
40 G. Gerth, P. Kienle and K. Luchner, *Phys. Lett. A*, 1968, **27**, 557–558.
41 M. W. Nathans and W. W. Wendlandt, *J. Inorg. Nucl. Chem.*, 1962, **24**, 869–879.
42 G. Corbel, M. Leblanc, E. Antic-Fidancev, M. Lemaître-Blaise and J. C. Krupa, *J. Alloys Compd.*, 1999, **287**, 71–78.
43 L. Pauling, *J. Am. Chem. Soc.*, 1929, **51**, 1010–1026.
44 G. M. Sheldrick, *Acta Crystallogr., Sect. A: Found. Crystallogr.*, 2008, **64**, 112–122.
45 G. J. Long, T. E. Cranshaw and G. Longworth, *Moessbauer Eff. Ref. Data J.*, 1983, **6**, 42.
46 R. A. Brand, *WinNormos for Igor6. Version for Igor 6.2 or above: 22.02.2017*, Universität Duisburg, Duisburg, Germany, 2017.
47 P. Netzsch, P. Gross, H. Takahashi, J. Brgoch, S. Lotfi and H. A. Höppe, in preparation.
48 S. G. Jantz, F. Pielnhofer, L. van Wüllen, R. Weihrich, M. J. Schäfer and H. A. Höppe, *Chem. – Eur. J.*, 2018, **24**, 443–450.